

Article

Accurate Nonstandard Path Integral Models for Arbitrary Dielectric Boundaries in 2-D NS-FDTD Domains

Tadao Ohtani ¹, Yasushi Kanai ²  and Nikolaos V. Kantartzis ^{3,*} ¹ Independent Researcher, Asahikawa 070-0841, Japan; bytcg100@ybb.ne.jp² Department of Engineering, Faculty of Engineering, Niigata Institute of Technology, Kashiwazaki 945-1195, Japan; kanai@iee.niit.ac.jp³ School of Electrical and Computer Engineering, Faculty of Engineering, Aristotle University of Thessaloniki, 541 24 Thessaloniki, Greece

* Correspondence: kant@auth.gr

Abstract: An efficient path integral (PI) model for the accurate analysis of curved dielectric structures on coarse grids via the two-dimensional nonstandard finite-difference time-domain (NS-FDTD) technique is introduced in this paper. In contrast to previous PI implementations of the perfectly electric conductor case, which accommodates orthogonal cells in the vicinity of curved surfaces, the novel PI model employs the occupation ratio of dielectrics in the necessary cells, providing thus a straightforward and instructive means to treat an assortment of practical applications. For its verification, the reflection from a flat plate and the scattering from a cylinder using the PI model are investigated. Results indicate that the featured methodology can enable the reliable and precise modeling of arbitrarily shaped dielectrics in the NS-FDTD algorithm on coarse grids.

Keywords: electromagnetic analysis; finite-difference time-domain methods; integral equations; numerical analysis; radar cross section



Citation: Ohtani, T.; Kanai, Y.; Kantartzis, N.V. Accurate Nonstandard Path Integral Models for Arbitrary Dielectric Boundaries in 2-D NS-FDTD Domains. *Sensors* **2024**, *24*, 2373. <https://doi.org/10.3390/s24072373>

Academic Editor: Ali Khenchaf

Received: 27 February 2024

Revised: 31 March 2024

Accepted: 7 April 2024

Published: 8 April 2024



Copyright: © 2024 by the authors. Licensee MDPI, Basel, Switzerland. This article is an open access article distributed under the terms and conditions of the Creative Commons Attribution (CC BY) license (<https://creativecommons.org/licenses/by/4.0/>).

1. Introduction

The nonstandard finite-difference time-domain (NS-FDTD) method is a high-accuracy analysis tool of the finite-difference (FD) type, proposed by Cole [1–3], to improve the performance of the FDTD algorithm [4,5]. The scheme, based on an FD Laplacian featured via the nonstandard (NS) concept, introduced by Mickens [6], can reduce the overall propagation error of a typical FDTD implementation by a factor of 10^{-4} on a coarse grid at a desired frequency [1,2]. Through these excellent characteristics, the NS-FDTD method is particularly suitable for the accurate computation of the radar cross section (RCS) of electrically large objects. Amid the most prominent applications of the NS-FDTD method, one may discern the full-scale analysis of aircrafts—whose electrical size is very large, namely, more than 500λ (λ is the wavelength)—with partially non-metal parts, including the radome, the canopy, the windows, and several radar-absorbing materials.

Nevertheless, the NS-FDTD method uses discrete space points to simulate electromagnetic wave propagation on orthogonal grids as in the FDTD technique [1–5]. Therefore, the discrete space treatment is unsuitable for realistic problems with arbitrarily shaped objects and fine details, not aligned to the grid axes [4,5,7–11], owing to the use of the insufficient staircase approximation on orthogonal grids in an effort to model the realistic object under study. Such structures can be, frequently, encountered in various applications, ranging from electromagnetic compatibility configurations [12–14] and microwave devices [15–17] to antennas [18–20], optical arrangements [21–25], and designs of low observability, including RCS scenarios. To circumvent such a drawback, a path integral (PI) model, based on the path integral form of Ampere’s and Faraday’s laws, has been previously presented [26–28]. The specific path integral scheme can effectively handle real-world objects on orthogonal

meshes, as the integral path may be intuitively placed on the object's surface. Thus, and owing to the PI model, the applicability of the NS-FDTD technique can be drastically expanded. However, the prior technique has been formulated only for the case of perfectly electric conductors (PECs); a fact that prohibits the analysis of various dielectric components found in many contemporary avionic and microwave telecommunication systems.

In this paper, a robust PI model for the rigorous treatment of dielectric objects, whose shape does not fit to any orthogonal grid, via the 2-D NS-FDTD method is developed. The proposed PI concept launches a simple scheme that considers the occupation ratio of all dielectrics at a specific cell. In this way, the manipulation of realistic dielectric structures becomes feasible on a coarse lattice. Firstly, to certify the key competence of the proposed PI model, we perform a reflection analysis of a flat plate and compare it with the exact solution. Next, an RCS problem is comprehensively explored via a real-world application. It is emphasized that for the NS-FDTD method, a practical grid width, Δ , is $\Delta \leq \lambda/8$. On the other hand, if dielectrics are involved in the computational domain, the modified grid width should be $\Delta' \leq \lambda/(8\sqrt{\epsilon_r})$ (ϵ_r is the relative dielectric permittivity). Furthermore, the use of a much finer lattice, i.e., $\Delta' \ll \Delta$, in order to satisfactorily treat the shape of a complicated structure, poses prohibitive issues in the implementation of the NS-FDTD method due to the unduly increase of the necessary system memory requirements and the extremely prolonged simulation times. These considerable drawbacks can be drastically circumvented by means of the proposed PI method, without the need for any additional conventions or non-physical assumptions, as occurs in existing schemes. Finally, all numerical outcomes reveal that the featured technique exhibits superior accuracy and convergence, as opposed to other computational approaches (with much finer spatial resolutions), for the trustworthy study of dielectric devices with intricate shape and elaborate geometrical features.

2. The PI Model at a Dielectric Boundary

2.1. Basics and Formulation

First, let us review the concept of the PI model for the NS-FDTD method [26–28]. The model uses both basic and complementary paths, as depicted in Figure 1, for the evaluation of the H_z magnetic-field component. Herein, we intend to establish a complementary relation between these two paths. The idea is based on the wave propagation characteristics of the Yee algorithm [1,2,5], where maximum and minimum errors occur at an angle of 45° on a square lattice. This indicates that we can mutually cancel these errors by means of two meshes for one node calculation. In an effort to attain the optimal cancellation of the inevitable discretization errors, the complementary (C) path is rotated 45° with respect to the basic (B) one. Specifically, the two integral paths are expressed as

$$\begin{aligned} \mu \int \frac{\partial \mathbf{H}}{\partial t} \cdot d\mathbf{S} &= - \int \mathbf{E} \cdot d\mathbf{l} \Rightarrow \mu \frac{\partial H_z^B(x, y)}{\partial t} \Delta^2 \\ &= - [E_y(x + \Delta/2, y) - E_x(x, y + \Delta/2) - E_y(x - \Delta/2, y) + E_x(x, y - \Delta/2)] \Delta, \end{aligned} \quad (1)$$

for the basic path, with $S = \Delta^2$ (Figure 1a), and

$$\begin{aligned} \mu \frac{\partial H_z^C(x, y)}{\partial t} 2\Delta^2 &= - [E_y^C(x + \Delta/2, y + \Delta/2) - E_x^C(x - \Delta/2, y + \Delta/2) \\ &\quad - E_y^C(x - \Delta/2, y - \Delta/2) + E_x^C(x + \Delta/2, y - \Delta/2)] \sqrt{2}\Delta, \end{aligned} \quad (2)$$

for the complementary path (Figure 1b). Note that in (1) and (2), we have replaced Δ with the nonstandard correction function $s_k(\Delta) = 2 \sin(k\Delta/2)/k$, where k is the physical wavenumber [1,2]. Based on this substitution, the propagation accuracy, $(k_n - k)/k$, of the basic and complementary path model is shown in Figure 2 for two lattice resolutions and k_n , representing the numerical wavenumber of the proposed PI model. The results are obtained via the method presented in [3,27], and as can be promptly observed, both models

exhibit opposite propagation errors for the desired mutual cancellation. In this manner, the new PI model is derived by means of

$$\frac{\partial H_z(x, y)}{\partial t} = \beta_0 \frac{\partial H_z^B(x, y)}{\partial t} + (1 - \beta_0) \frac{\partial H_z^C(x, y)}{\partial t}, \quad (3)$$

where, for homogeneous media, β_0 is given by [26]

$$\beta_0 \approx \frac{2}{3} - \frac{(k\Delta)^2}{90}. \quad (4)$$

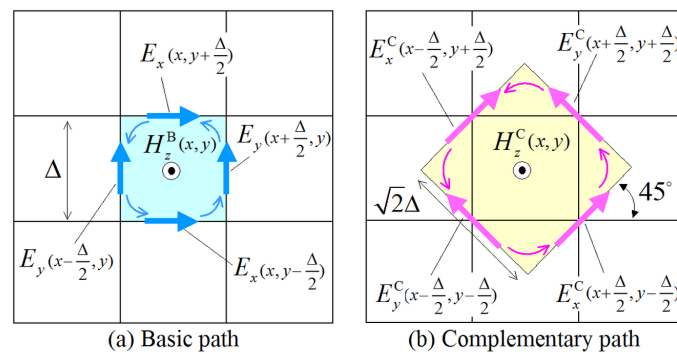


Figure 1. The two paths—(a) basic and (b) complementary—involved in the proposed integral NS-FDTD form for the calculation H_z magnetic-field component on a square lattice. The two paths are rotated 45° , one with regard to the other, in order to mutually cancel their discretization errors.

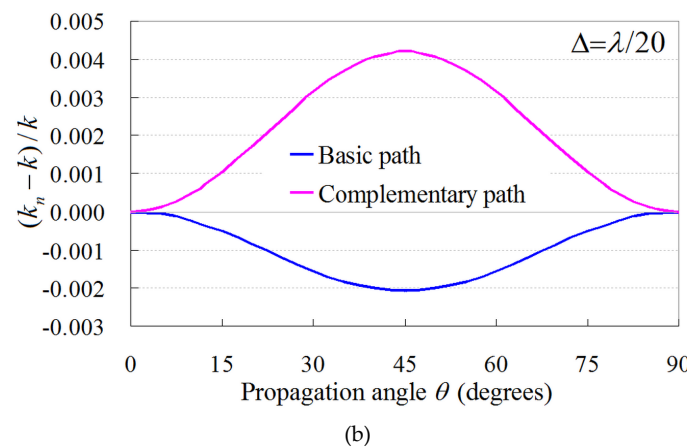
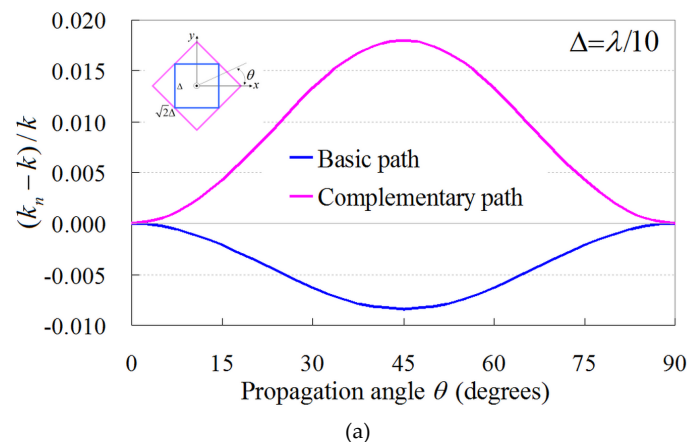


Figure 2. Propagation accuracy of the basic and complementary PI model using the nonstandard correction function $s_k(\Delta) = 2 \sin(k\Delta/2)/k$ for (a) $\Delta = \lambda/10$ and (b) $\Delta = \lambda/20$.

On the dielectric surface, we select the first term of (4), i.e., $\beta_0 = 2/3$, which is independent of the k , as the latter varies across the dielectric boundary. Additionally, in (3), we consider $\partial H_z/\partial t = (H_z^{n+1} - H_z^n)/s_\omega(\Delta t)$, with $s_\omega(\Delta t) = 2 \sin(\omega\Delta/2)/\omega$, from the nonstandard formulation of [1,2], ω is the angular frequency, Δt is the time step, and $n = t/\Delta t$. On the other hand, the E_y^C term in (2) is obtained from the already known $E_{x,y}$ values on the basic path as

$$E_y^C(x + \Delta/2, y + \Delta/2) = \frac{1}{2} \{ [E_x(x, y + \Delta/2) + E_x(x + \Delta, y + \Delta/2)] \mathbf{e}_x + [E_y(x + \Delta/2, y) + E_y(x + \Delta/2, y + \Delta)] \mathbf{e}_y \} \cdot \frac{-\mathbf{e}_x + \mathbf{e}_y}{\sqrt{2}}, \quad (5)$$

where $\mathbf{e}_{x,y}$ are the corresponding unit vectors. Bear in mind that an analogous expression for the E_x^C term can be similarly obtained.

2.2. Treatment of the Magnetic-Field Components

The new PI model of (1) and (2) is, now, extended to the treatment of the definitely more demanding dielectric boundaries. Therefore, based on the geometric depiction of the proposed PI for such a scenario, the $\mu \int (\partial \mathbf{H}/\partial t) \cdot d\mathbf{S} = - \int \mathbf{E} \cdot d\mathbf{l}$ along the basic path in Figure 3 is given by

$$\begin{aligned} \mu \frac{\partial H_z^B}{\partial t} (S_{B0} + S_{B1}) = & - [E_y(x + \Delta/2, y) l_0 - E_y(x - \Delta/2, y) l_1 \\ & - E_x(x, y + \Delta/2)_{\varepsilon_0} (1 - \delta_{B1}) l_0 - E_x(x, y + \Delta/2)_{\varepsilon_1} \delta_{B1} l_1 \\ & + E_x(x, y - \Delta/2)_{\varepsilon_0} (1 - \delta_{B2}) l_0 + E_x(x, y - \Delta/2)_{\varepsilon_1} \delta_{B2} l_1], \end{aligned} \quad (6)$$

where $l_{0,1} \equiv s_{k_{0,1}}(\Delta) = 2 \sin(k_{0,1}\Delta/2)/k_{0,1}$ with $k_{0,1}$ as the wavenumber of the $\varepsilon_{0,1}$ dielectric medium, $S_{B0,B1}$ are the areas occupied by the $\varepsilon_{0,1}$ dielectric medium inside the basic path, and $\delta_{B1,B2}$ are path lengths along the basic path in the ε_1 medium. Also, the $E_{x,y}(x, y)_{\varepsilon_{0,1}}$ notation refers to the $E_{x,y}$ component in the $\varepsilon_{0,1}$ dielectric medium. Note that if $E_{x,y}$ is not available at a specific node on the grid, we use the $E_{x,y}$ extrapolation values at the nearest-neighbor node; for example, $E_x(x, y + \Delta/2)_{\varepsilon_1} \sim E_x(x - \Delta, y + \Delta/2)$. Similarly, the $\partial H_z^C/\partial t$ term using the complementary path in Figure 3 is given by

$$\begin{aligned} \mu \frac{\partial H_z^C}{\partial t} (S_{C0} + S_{C1}) = & - [E_y^C(x + \Delta/2, y + \Delta/2)_{\varepsilon_1} \sqrt{2} l_0 - E_y^C(x - \Delta/2, y - \Delta/2)_{\varepsilon_0} \delta_{C2} l_0 \\ & - E_y^C(x - \Delta/2, y - \Delta/2)_{\varepsilon_1} (\sqrt{2} - \delta_{C2}) l_1 - E_x^C(x - \Delta/2, y + \Delta/2)_{\varepsilon_1} (\sqrt{2} - \delta_{C1}) l_1 \\ & - E_x^C(x - \Delta/2, y + \Delta/2)_{\varepsilon_0} \delta_{C1} l_0 + E_x^C(x + \Delta/2, y - \Delta/2)_{\varepsilon_1} l_0]. \end{aligned} \quad (7)$$

It should be stressed that for the practical application of (7), we assume that the $E_{x,y}^C(x, y)_{\varepsilon_{0,1}}$ terms exist on the integral path that straddles the dielectric boundary. In this manner, we can project the already known $E_{x,y}(x, y)$ values to the corresponding $\mathbf{e}_{x,y}$ directional unit vector on the integral path. For illustration, the $E_x^C(x - \Delta/2, y + \Delta/2)_{\varepsilon_0}$ term in (7) is obtained from the $E_x(x, y + \Delta/2) \mathbf{e}_x \cdot (\mathbf{e}_x + \mathbf{e}_y)/\sqrt{2}$ projection. Then, and similarly to (5), the $E_x^C(x - \Delta/2, y + \Delta/2)_{\varepsilon_1}$ term in (7) is acquired from the inner product of $\{E_x(x - \Delta, y + \Delta/2) \mathbf{e}_x + [E_y(x - \Delta/2, y) + E_y(x - \Delta/2, y + \Delta)] \mathbf{e}_y/2\} \cdot (\mathbf{e}_x + \mathbf{e}_y)/\sqrt{2}$, with an analogous treatment holding for the other E^C terms, as well. Having determined the $\partial H_z^B/\partial t$ and $\partial H_z^C/\partial t$ quantities from (6) and (7), respectively, the required $\partial H_z/\partial t$ derivative is evaluated by means of (3).

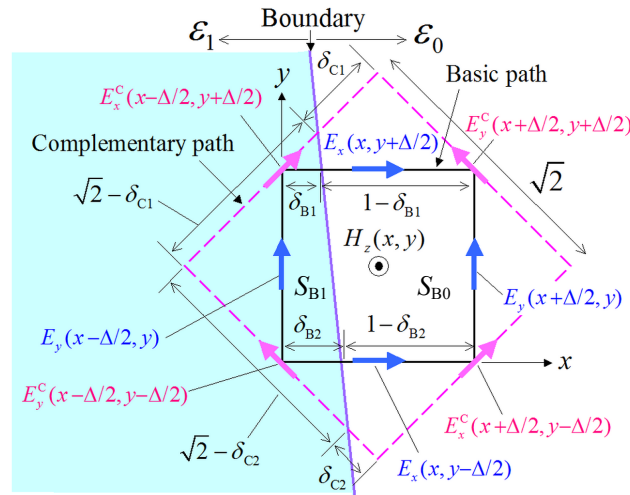


Figure 3. The proposed PI model for the calculation of the H_z component at a $\Delta \times \Delta$ lattice in the case of a dielectric boundary between an ε_0 and an ε_1 medium. The path length is measured via the $s_k(\Delta)$ nonstandard correction function [1,2]. Moreover, $S_{B0,B1}$ are the areas occupied by the $\varepsilon_{0,1}$ dielectric medium inside the basic path, $\delta_{B1,B2}$ are path lengths along the basic path in the ε_1 medium, and $\delta_{C1,C2}$ are path lengths along the complementary path in the ε_0 medium.

2.3. Treatment of the Electric-Field Components

The most frequently encountered cases for the computation of electric-field quantities at a dielectric boundary are those of a normal E_x and a parallel E_y component with regard to the boundary, as described in Figure 4. In particular, concentrating on Figure 4a and in terms of $\varepsilon \int (\partial \mathbf{E} / \partial t) \cdot d\mathbf{S} = \int \mathbf{H} \cdot d\mathbf{l}$, we derive

$$E_x^{n+1/2}(x, y + \Delta/2) = E_x^{n-1/2}(x, y + \Delta/2) + \text{ch}_n [H_z^n(x, y + \Delta) - H_z^n(x, y)], \quad (8)$$

for

$$\text{ch}_n = \delta \text{ch}_1 + (1 - \delta) \text{ch}_0, \quad \text{ch}_1 = \frac{s_\omega(\Delta t)}{\varepsilon_1 s_{k_1}(\Delta)}, \quad \text{ch}_0 = \frac{s_\omega(\Delta t)}{\varepsilon_0 s_{k_0}(\Delta)}. \quad (9)$$

Moreover, for the scenario of Figure 4b, one acquires

$$E_y^{n+1/2}(x + \Delta/2, y) = E_y^{n-1/2}(x + \Delta/2, y) - \text{ch}_p [H_z^n(x + \Delta, y) s_{k_0}(\Delta) - H_z^n(x, y) s_{k_1}(\Delta)], \quad (10)$$

for

$$\text{ch}_p = \frac{s_\omega(\Delta t)}{\delta \varepsilon_1 s_{k_1}^2(\Delta) + (1 - \delta) \varepsilon_0 s_{k_0}^2(\Delta)}. \quad (11)$$

On the other hand, when the case of an obliquely aligned, with respect to the lattice, dielectric boundary is taken into account, we introduce the cell division scheme of Figure 5, where $A_{\delta,\varepsilon}$ is the occupied area ratio. Explicitly, Figure 5a is considered as the parallel case of Figure 4b, while the entire model in Figure 5a,b is treated as the normal case of Figure 4a. Hence, the corresponding $\partial E_x / \partial t$ can be expressed as

$$E_x^{n+1/2}(x, y + \Delta/2) = E_x^{n-1/2}(x, y + \Delta/2) - \delta_x \text{ch}_a [H_z^n(x, y + \Delta) s_{k_0}(\Delta) - H_z^n(x, y) s_{k_1}(\Delta)] \\ + (1 - \delta_x) \text{ch}_0 [H_z^n(x, y + \Delta) - H_z^n(x, y)], \quad (12)$$

for

$$\text{ch}_a = \frac{s_\omega(\Delta t)}{\varepsilon_1 s_{k_1}(\Delta) A_{\delta, \varepsilon_1} + \varepsilon_0 s_{k_0}(\Delta) A_{\delta, \varepsilon_0}}, \quad (13)$$

with a similar formula holding for the $\partial E_y / \partial t$ temporal derivative. In addition, the $E_{x,y}^C$ components on the complementary path can be extracted through the inner products of these $E_{x,y}$ components with the respective unit vector $\mathbf{u}_{x,y} = (\mathbf{e}_y \pm \mathbf{e}_x) / \sqrt{2}$. Notice that (8)–(13) are the best models, derived theoretically and numerically from the previous analysis. Finally, as a supplement, a special case of the right-angle edge can be treated by (i) selecting the Δ width, so that the edge fits on the grid, (ii) moving the edge to the grid line, so that it fits on, and (iii) applying the modified PI models of Figures 4 and 5.

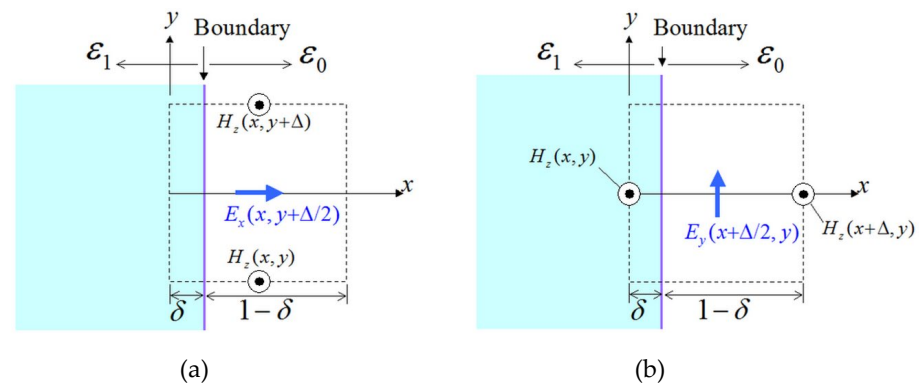


Figure 4. Treatment of a (a) normal E_x component and (b) parallel E_y component with respect to the dielectric boundary. Here, δ is the occupation ratio equal to the area of the ε_1 medium over the entire area of a cell.

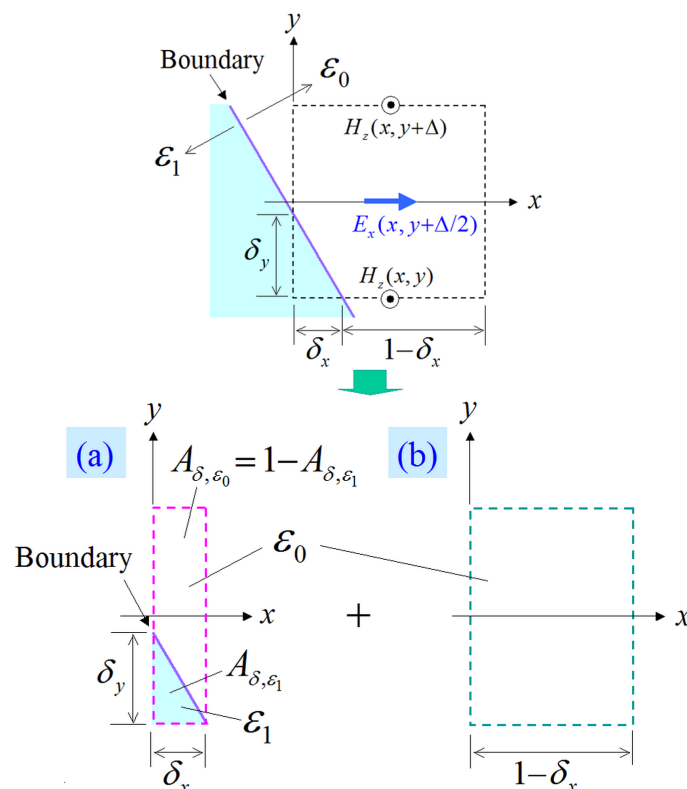


Figure 5. Division model of an E_x cell to treat an oblique dielectric boundary. The boundary case for the E_x cell is divided into (a) the parallel case and (b) the free-space case.

3. Numerical Results and Discussion

3.1. Reflectivity Analysis of a Flat Dielectric Plate

In order to substantiate the merits of the featured PI model, we focus on the reflectivity analysis of a flat dielectric plate as a basic example with an analytic solution. The computational domain is shown in Figure 6, whereas the PI models of (5)–(13) are employed only on the dielectric surface. Moreover, the plate is infinite along the $\pm y$ directions, and an incident plane wave impinges from the right side in Figure 6. Therefore, the sine–cosine method [29] is used for our oblique incidence calculations. For our (TM = (H_x, H_y, E_z)) and TE = (E_x, E_y, H_z)) analysis, we examine two dielectric media, namely, an acrylic resin with $\epsilon_1 = 3\epsilon_0$ and a glass epoxy with $\epsilon_1 = 4\epsilon_0$. The remaining implementation aspects are: $\lambda = 1$ m, $\Delta = \lambda/20$, and $\Delta t = T/30$, with T as the corresponding wave period, while open-space truncation is conducted in terms of a 15Δ -thick perfectly matched layer (PML) [30]. To facilitate our comparisons, we use, as our reference, the analytical solution of the specific problem described in [31]. In this context, Figure 7 illustrates the reflectivity of the flat dielectric plate for the aforementioned materials and two Δw configurations, i.e., $\Delta w = 0$ (the right-hand side of the plate surface is aligned to the grid) and $\Delta w = \Delta/4$ (the plate surface is not aligned to the grid). As observed, all the outcomes derived via the enhanced PI models are in promising agreement with the reference solution, thus proving the competence of the new scheme to effectively treat arbitrary dielectric boundaries. In this case, the flat plate model can be treated accurately for a geometrical integral path length and occupied ratio in the cell since the dielectric boundary is straight and parallel to the grid line (y -axis). Hence, we can detect that the PI model closely follows the analytic solution if we utilize an exact path length and occupied ratio in the PI cell. This fact proves the validity of the proposed PI model in the analysis of arbitrary dielectric boundaries.

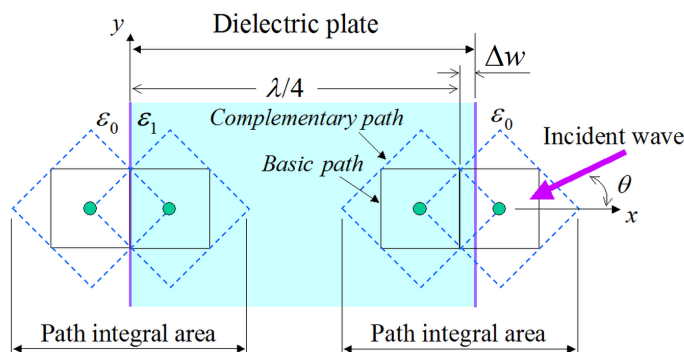


Figure 6. Reflectivity evaluation of a flat dielectric plate by means of the proposed PI model, where, except for the PI area, the rest of the domain is a differential type NS-FDTD region. Note that Δw is the distance between the grid line of the basic path and the plate edge, with $\Delta w = 0$ at the left side. The dielectric plate is infinite along the $\pm y$ directions with a thickness of $\lambda/4 + \Delta w$.

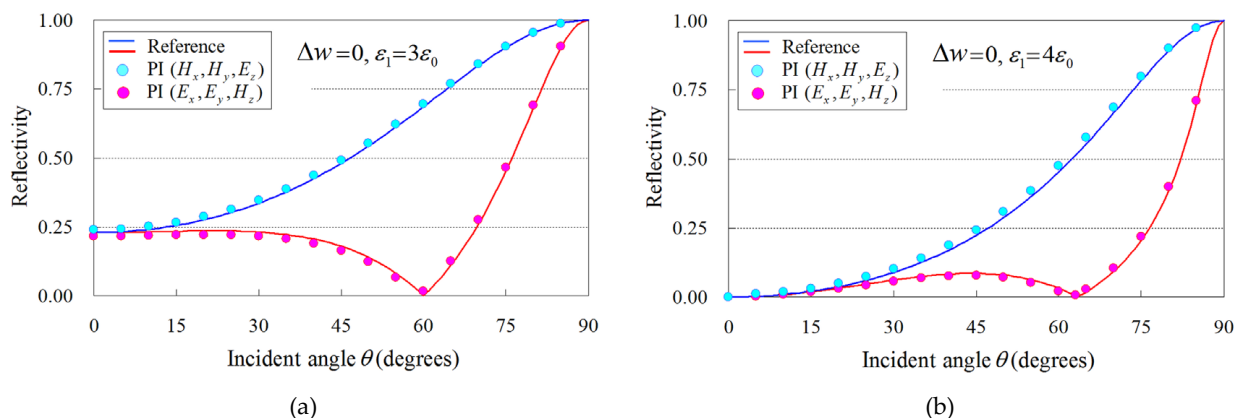


Figure 7. Cont.

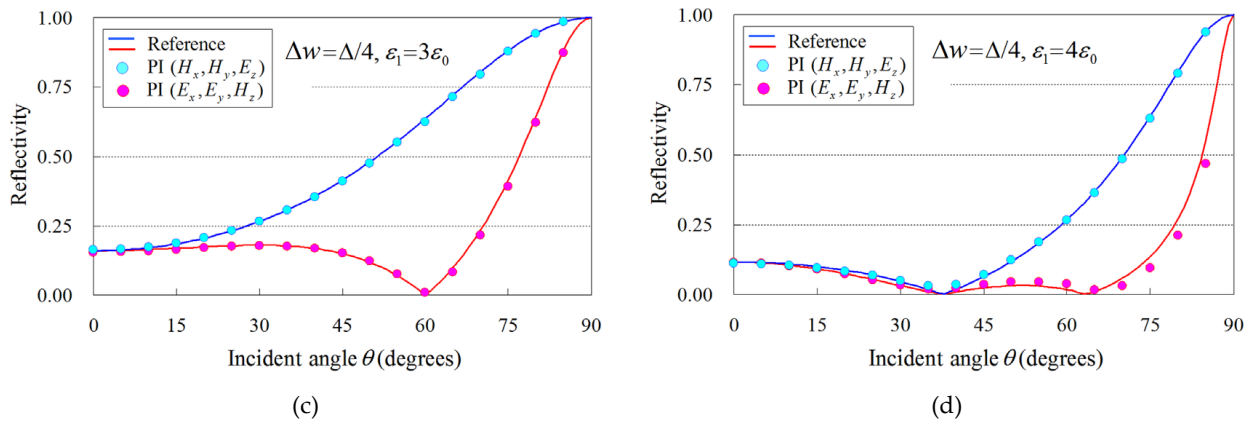


Figure 7. Reflectivity (TM = (H_x, H_y, E_z) and TE = (E_x, E_y, H_z)) analysis versus the incidence angle, θ , for the flat dielectric plate of Figure 6, performed in terms of the proposed PI model and compared to the analytical (reference) solution of [31]. The analysis involves two dielectric media (acrylic resin and glass epoxy) in conjunction with two Δw arrangements ($\Delta w = 0$: the right-hand side of the plate surface is aligned to the grid and $\Delta w = \Delta/4$: the plate surface is not aligned to the grid). (a) Acrylic resin with $\varepsilon_1 = 3\varepsilon_0$ and $\Delta w = 0$, (b) glass epoxy with $\varepsilon_1 = 4\varepsilon_0$ and $\Delta w = 0$, (c) acrylic resin with $\varepsilon_1 = 3\varepsilon_0$ and $\Delta w = \Delta/4$, and (d) glass epoxy with $\varepsilon_1 = 4\varepsilon_0$ and $\Delta w = \Delta/4$.

3.2. RCS Analysis of a Dielectric Cylinder

Probing further, we proceed to a more realistic application and compute the RCS of an infinite dielectric cylinder with a radius of 5Δ and a relative permittivity of $\varepsilon_r = 3$. For the curved boundary, we utilize the oblique dielectric models of Figure 5, formulated in (6)–(13). The grid layout is given in Figure 8, where the novel PI model is applied only on the cylinder surface and the rest of the domain is a regular NS-FDTD region. In particular, Figure 8a depicts the PI model of the H_z component, expressed via (3), (6), and (7), while Figure 8b presents the PI model for the E_x component, described by (8)–(13). This configuration is attributed to the occupation ratio of the dielectrics and the direction of the electric field in the shaded (cyan) cells. Note that the treatment of the E_y component is the same as the E_x one, owing to the rotational symmetry of the problem. Furthermore, for the excitation of the structure through an incident plane wave (impinging with an angle of $\theta = 45^\circ$) and the evaluation of the scattered waves from the dielectric cylinder, the total-field/scattered-field formulation [5] is employed. Finally, the scattered waves, so obtained, are converted to the appropriate RCS data by means of the near-to-far-field transformation technique [5,31].

In this framework, Figure 9 illustrates the comparative results between our model (PI model combined with the NS-FDTD technique: PI+NS-FDTD) and other approaches (typical FDTD and NS-FDTD method without the PI model) for $\lambda = 1$ m, $\Delta = \lambda/14$, and $\Delta t = T/20$. Also, the outcomes of a much finer FDTD implementation ($\Delta = \lambda/84$, $\Delta t = T/120$) serve as our reference solution. It becomes apparent that the PI+NS-FDTD method agrees very well with the reference data within the range of 0.5 dBm, which is, actually, a negligible difference in most real-world RCS configurations. Herein, the reduction effect is $(14/84)^2$ for the overall computer memory and the same analysis space size since the reference FDTD solution uses a $\Delta = \lambda/84$ and the NS-FDTD simulation with the PI model employs a $\Delta = \lambda/14$. Additionally, our method achieves a reduction effect of $(14/84)^2 \times (20/120)$ for the total CPU time, compared with the FDTD algorithm, because the reference FDTD solution uses a $\Delta t = T/120$, while the NS-FDTD simulation with the PI model employs a $\Delta t = T/20$. In Figure 9, a small fluctuation of 0.5 dBm is observed in the PI results for the observation angle θ . This small discrepancy can be attributed to the geometrical layout of the PI cell in Figure 8, as the PI models periodically vary regarding the cylinder surface position. To mitigate this RCS fluctuation, one may use finer cells, as deduced from the FDTD results with $\Delta = \lambda/14$ and $\Delta = \lambda/84$, since the specific PI model robustly replaces the complicated scattering phenomena on the cylinder surface

(smaller than $\Delta \times \Delta$) with one cell calculation on the coarse grid. However, it should be emphasized that the RCS fluctuation versus the observation angle is much smaller than that of the NS-FDTD simulation without the PI model. Lastly, regarding the bistatic RCS for $\theta = 45^\circ$, our scheme offers, again, a very satisfactory performance, as shown in Figure 10, for the same set of implementation parameters as in the prior example. It should be stated that only a small RCS fluctuation is detected in the PI outcomes. Bear in mind that if a sufficiently fine (i.e., $\Delta = \lambda/20$) cell is selected in Figure 8, such fluctuations are not at all observed. This implies that the fluctuations in Figure 10 are attributed to the use of the $\Delta = \lambda/(8\sqrt{\epsilon_r})|_{\epsilon_r=3} \sim \lambda/14$ maximum grid size [1,2] and the geometrical layout of the PI cell, as already mentioned in the monostatic case. Consequently, the novel formulation can reliably and accurately treat the curved shape of dielectric structures, even when their surface is not aligned to the axes of orthogonal NS-FDTD grids.

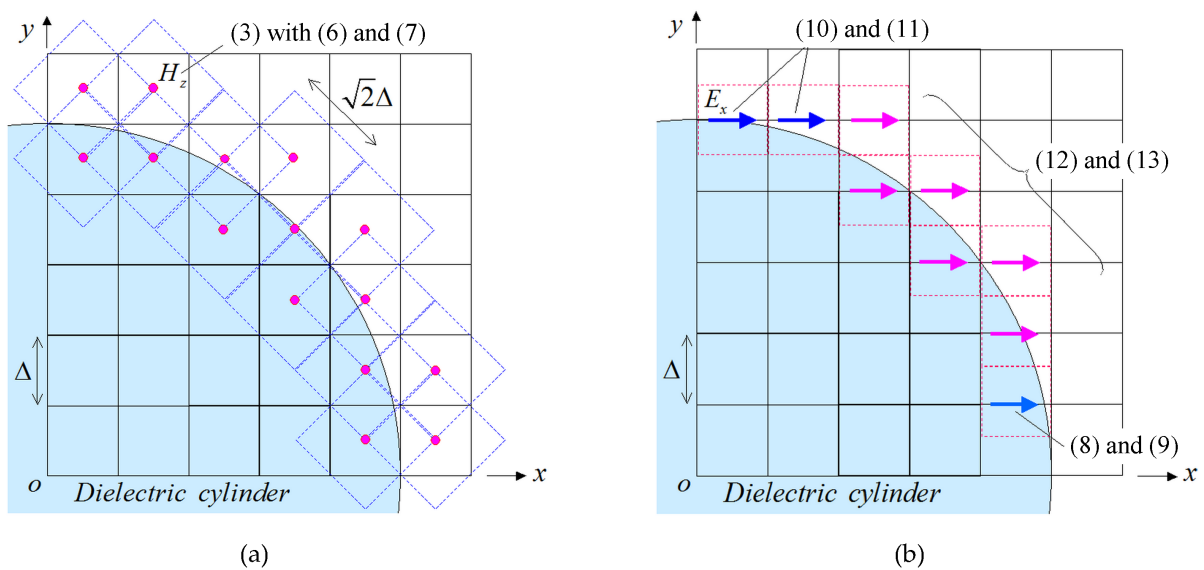


Figure 8. The PI model of an infinite dielectric cylinder (first quadrant) for the TE mode with the positions of the involved (a) H_z components, computed through (3), (6), and (7), and (b) E_x components, calculated via (8)–(13). The proposed scheme is used solely on the cylinder surface, while the remaining domain is a typical NS-FDTD region. Note that due to rotational symmetry, the E_y case is similar to the E_x one.

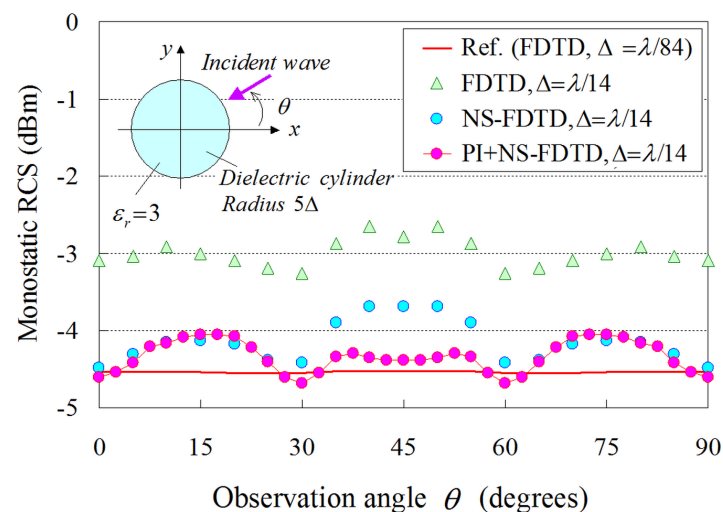


Figure 9. Monostatic RCS results derived from the proposed (PI+NS-FDTD) technique, the conventional FDTD method, and the NS-FDTD algorithm without the PI model. The reference solution is acquired from an FDTD realization with a very fine ($\Delta = \lambda/84$, $\Delta t = T/120$) lattice resolution.

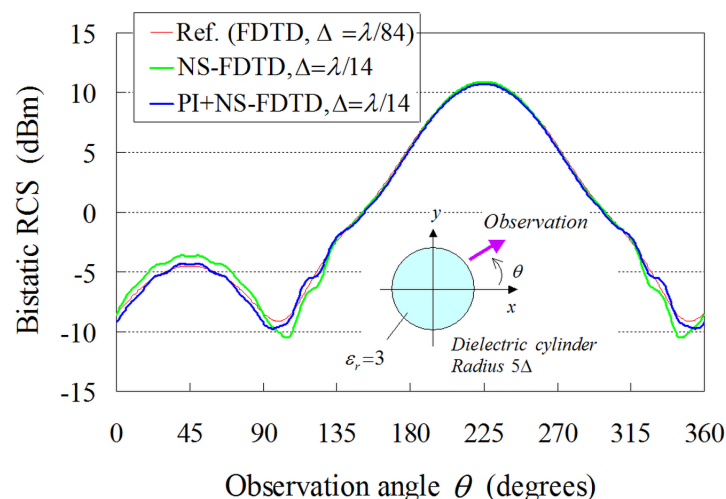


Figure 10. Bistatic RCS results derived from the proposed (PI+NS-FDTD) technique and the NS-FDTD algorithm without the PI model. The reference solution is acquired from an FDTD realization with a very fine ($\Delta = \lambda/84$, $\Delta t = T/120$) lattice resolution. The incidence angle of the impinging plane wave is 45° , while the geometric PI cell data of the cylinder are depicted in Figure 8.

4. Conclusions

Conventional grid-based computational methods exhibit significant precision issues since they are not able to efficiently model curved media boundaries. To alleviate these shortcomings and accurately handle dielectric objects of an arbitrary shape, not aligned to the grid axes, a consistent and efficient PI form for the 2-D NS-FDTD technique has been presented in this paper. The key idea of the proposed PI scheme is to utilize the occupation ratio of dielectrics in the necessary cells, surrounded by basic and complementary paths, thus attaining a notable reduction of the overall system burden. Conducting the numerical RCS analysis of a dielectric plate and cylinder, it has been validated that the new concept improves the accuracy of the regular NS-FDTD algorithm in the case of dielectric boundaries, considerably curved interfaces, and fine geometric characteristics. Thus, the universality of the NS-FDTD technique can be seriously expanded, even on coarse grids, without having to resort to any additional complicated approaches or artificial assumptions. Specifically, for the demanding RCS study of electrically large configurations (partially occupied by various dielectrics), which opt for excessive memory requirements and elongated simulations, the new PI model is proven to offer remarkable computational savings. Nonetheless, it should be stated that generating the appropriate geometrical data for the PI model is a laborious task from a calculation point of view. Therefore, for a beneficial real-world use of the featured scheme, the development of a CAD tool is deemed necessary.

Author Contributions: Conceptualization, N.V.K.; Funding acquisition, Y.K.; Methodology, T.O.; Software, T.O.; Supervision, Y.K.; Visualization, T.O.; Writing—review and editing, Y.K. and N.V.K. All authors have read and agreed to the published version of the manuscript.

Funding: This research received no external funding.

Institutional Review Board Statement: Not applicable.

Informed Consent Statement: Not applicable.

Data Availability Statement: Data are contained within the article.

Conflicts of Interest: The authors declare no conflicts of interest.

References

1. Cole, J. A high accuracy FDTD algorithm to solve microwave propagation and scattering problems on a coarse grid. *IEEE Trans. Microw. Theory Tech.* **1995**, *43*, 2053–2058. [\[CrossRef\]](#) [\[CrossRef\]](#)
2. Cole, J. High-accuracy Yee algorithm based on nonstandard finite differences: New developments and verifications. *IEEE Trans. Antennas Propag.* **2002**, *50*, 1185–1191. [\[CrossRef\]](#) [\[CrossRef\]](#)
3. Ohtani, T.; Kanai, Y. Coefficients of finite difference operator for rectangular cell NS-FDTD method. *IEEE Trans. Antennas Propag.* **2011**, *59*, 206–213. [\[CrossRef\]](#) [\[CrossRef\]](#)
4. Kunz, K.S.; Luebbers, R.J. *The Finite Difference Time Domain Method for Electromagnetics*; CRC Press: New York, NY, USA, 1993; Chapter 13.
5. Taflov, A.; Hagness, S.C. *Computational Electrodynamics: The Finite-Difference Time-Domain Method*, 3rd ed.; Artech House: Norwood, MA, USA, 2005; Chapter 3, 10, 11.
6. Mickens, R.E. *Nonstandard Finite Difference Models of Differential Equations*; World Scientific: Singapore, 1984.
7. Liu, Y.; Shi, L.; Wang, J.; Chen, H.; Lei, Q.; Duan, Y.; Zhang, Q.; Fu, S.; Sun, Z. TO-FDTD method for arbitrary skewed periodic structures at oblique incidence. *IEEE Trans. Microw. Theory Tech.* **2020**, *68*, 564–572. [\[CrossRef\]](#) [\[CrossRef\]](#)
8. Valverde, A.M.; Cabello, M.R.; Sánchez, C.C.; Bretones, A.R.; Garcia, S.G. On the effect of grid orthogonalization in stability and accuracy of an FDTD subgridding method. *IEEE Trans. Antennas Propag.* **2022**, *70*, 10769–10776. [\[CrossRef\]](#) [\[CrossRef\]](#)
9. Ruiz Cabello, M.; Martín Valverde, A.J.; Plaza, B.; Frövel, M.; Poyatos, D.; Bretones, A.R.; Bravo, A.G.; García, S.G. A subcell finite-difference time-domain implementation for narrow slots on conductive panels. *Appl. Sci.* **2023**, *13*, 8949. [\[CrossRef\]](#) [\[CrossRef\]](#)
10. Xu, P.; Liu, J. Iteration-based temporal subgridding method for the finite-difference time-domain algorithm. *Mathematics* **2024**, *12*, 302. [\[CrossRef\]](#) [\[CrossRef\]](#)
11. Bahrami, A.; Deck-Léger, Z.L.; Li, Z.; Caloz, C. A generalized FDTD scheme for moving electromagnetic structures with arbitrary space–time configurations. *IEEE Trans. Antennas Propag.* **2024**, *72*, 1721–1734. [\[CrossRef\]](#) [\[CrossRef\]](#)
12. Shi, W.; Wang, J.; Wang, Y.; Huo, J.J.; Yin, W.Y. An area-averaged conformal technique for the electromagnetic simulations of Debye medium. *IEEE Trans. Electromagn. Compat.* **2022**, *64*, 1978–1985. [\[CrossRef\]](#) [\[CrossRef\]](#)
13. Ye, Z.; Shi, Y.; Gao, Z.; Wu, X. Time-domain hybrid method for the coupling analysis of power line network with curved and multidirectional segments. *IEEE Trans. Electromagn. Compat.* **2023**, *65*, 216–224. [\[CrossRef\]](#) [\[CrossRef\]](#)
14. Tong, X.; Sun, Y. A hybrid Chebyshev pseudo-spectral finite-difference time-domain method for numerical simulation of 2D acoustic wave propagation. *Mathematics* **2024**, *12*, 117. [\[CrossRef\]](#) [\[CrossRef\]](#)
15. Navarro, E.A.; Portí, J.A.; Salinas, A.; Navarro-Modesto, E.; Toledo-Redondo, S.; Fornieles, J. Design & optimization of large cylindrical radomes with subcell and non-orthogonal FDTD meshes combined with genetic algorithms. *Electronics* **2021**, *10*, 2263. [\[CrossRef\]](#) [\[CrossRef\]](#)
16. Takahashi, K.; Aoike, K.; Ono, M.; Yoneda, J. Robust estimation of the dielectric constant of cylindrical objects using wideband radar transmission measurements. *IEEE Trans. Microw. Theory Tech.* **2022**, *70*, 3666–3674. [\[CrossRef\]](#) [\[CrossRef\]](#)
17. Wang, Y.; Xie, Y.; Jiang, H.; Wu, P. Narrow-bandpass one-step leapfrog hybrid implicit-explicit algorithm with convolutional boundary condition for its applications in sensors. *Sensors* **2022**, *22*, 4445. [\[CrossRef\]](#) [\[CrossRef\]](#) [\[PubMed\]](#)
18. Kazemzadeh, M.R.; Broderick, N.G.R.; Xu, W. Novel time-domain electromagnetic simulation using triangular meshes by applying space curvature. *IEEE Open J. Antennas Propag.* **2020**, *1*, 387–395. [\[CrossRef\]](#) [\[CrossRef\]](#)
19. Mao, Y.; Zhan, Q.; Wang, D.; Zhang, R.; Liu, Q.H. Modeling thin 3-D material surfaces using a spectral-element spectral-integral method with the surface current boundary condition. *IEEE Trans. Antennas Propag.* **2022**, *70*, 2375–2380. [\[CrossRef\]](#) [\[CrossRef\]](#)
20. David, D.S.K.; Jeong, Y.; Wu, Y.C.; Ham, S. An analytical antenna modeling of electromagnetic wave propagation in inhomogeneous media using FDTD: A comprehensive study. *Sensors* **2023**, *23*, 3896. [\[CrossRef\]](#) [\[CrossRef\]](#) [\[PubMed\]](#)
21. Samak, M.M.E.A.; Bakar, A.A.A.; Kashif, M.; Zan, M.S.D. Comprehensive numerical analysis of finite difference time domain methods for improving optical waveguide sensor accuracy. *Sensors* **2016**, *16*, 506. [\[CrossRef\]](#) [\[CrossRef\]](#)
22. Fu, Y.; Yager, T.; Chikvaidze, G.; Iyer, S.; Wang, Q. Time-resolved FDTD and experimental FTIR study of gold micropatch arrays for wavelength-selective mid-infrared optical coupling. *Sensors* **2021**, *21*, 5203. [\[CrossRef\]](#) [\[CrossRef\]](#) [\[PubMed\]](#)
23. Wu, X.; Xiao, J. Improved full-vectorial meshfree mode solver for step-index optical waveguides with arbitrary dielectric interfaces. *J. Lightw. Technol.* **2022**, *40*, 4746–4757. [\[CrossRef\]](#) [\[CrossRef\]](#)
24. Yang, X.; Xia, D.; Li, J.; Chu, Q. Highly sensitive micro-opto-electromechanical systems accelerometer based on MIM waveguide wavelength modulation. *IEEE Sens. J.* **2023**, *23*, 181–188. [\[CrossRef\]](#) [\[CrossRef\]](#)
25. Jannesari, R.; Pühringer, G.; Stocker, G.; Grille, T.; Jakob, B. Design of a high Q-factor label-free optical biosensor based on a photonic crystal coupled cavity waveguide. *Sensors* **2024**, *24*, 193. [\[CrossRef\]](#) [\[CrossRef\]](#) [\[PubMed\]](#)
26. Ohtani, T.; Kanai, Y.; Kantartzis, N.V. A rigorous path integral scheme for the two-dimensional nonstandard finite-difference time-domain method. In Proceedings of the 22nd IEEE Conference on the Computation of Electromagnetic Fields (COMPUMAG), Paris, France, 15–19 July 2019; pp. PA–M4–9(1–2).
27. Ohtani, T.; Kanai, Y.; Kantartzis, N.V. A nonstandard path integral model for curved surface analysis. *Energies* **2022**, *15*, 4322. [\[CrossRef\]](#) [\[CrossRef\]](#)
28. Ohtani, T.; Kanai, Y.; Kantartzis, N.V. A path integral representation model to extend the analytical capability of the nonstandard finite-difference time-domain method. *ACES J.* **2024**, *in press*.

-
29. Taflove, A. *Advances in Computational Electrodynamics: The Finite-Difference Time-Domain Method*; Artech House: Norwood, MA, USA, 1998; Chapter 6.
 30. Bérenger, J.P. *Perfectly Matched Layer (PML) for Computational Electromagnetics*; Springer Nature: New York, NY, USA, 2007.
 31. Balanis, C.A. *Advanced Engineering Electromagnetics*, 2nd ed.; John Wiley & Sons: New York, NY, USA, 2012; Chapter 5.

Disclaimer/Publisher's Note: The statements, opinions and data contained in all publications are solely those of the individual author(s) and contributor(s) and not of MDPI and/or the editor(s). MDPI and/or the editor(s) disclaim responsibility for any injury to people or property resulting from any ideas, methods, instructions or products referred to in the content.